

Central Lancashire Online Knowledge (CLOK)

Title	Micromagnetic study of spin transport in easy-plane antiferromagnetic insulators
Type	Article
URL	https://clock.uclan.ac.uk/45027/
DOI	https://doi.org/10.1103/PhysRevB.107.184404
Date	2023
Citation	Brehm, Verena, Gomonay, Olena, Lepadatu, Serban, Klau, Mathias, Sinova, Jairo, Brataas, Arne and Qaiumzadeh, Alireza (2023) Micromagnetic study of spin transport in easy-plane antiferromagnetic insulators. Physical Review B. pp. 107-18. ISSN 2469-9950
Creators	Brehm, Verena, Gomonay, Olena, Lepadatu, Serban, Klau, Mathias, Sinova, Jairo, Brataas, Arne and Qaiumzadeh, Alireza

It is advisable to refer to the publisher's version if you intend to cite from the work.
<https://doi.org/10.1103/PhysRevB.107.184404>

For information about Research at UCLan please go to <http://www.uclan.ac.uk/research/>

All outputs in CLOK are protected by Intellectual Property Rights law, including Copyright law. Copyright, IPR and Moral Rights for the works on this site are retained by the individual authors and/or other copyright owners. Terms and conditions for use of this material are defined in the <http://clock.uclan.ac.uk/policies/>


Micromagnetic study of spin transport in easy-plane antiferromagnetic insulators

Verena Brehm^{1,*}, Olena Gomonay², Serban Lepadatu³, Mathias Kläui^{1,2}, Jairo Sinova²,
Arne Brataas¹, and Alireza Qaiumzadeh¹

¹*Center for Quantum Spintronics, Department of Physics, Norwegian University of Science and Technology, Høgskoleringen 5, 7491 Trondheim, Norway*

²*Institute of Physics, Johannes Gutenberg-University Mainz, Staudingerweg 7, Mainz 55128, Germany*

³*Jeremiah Horrocks Institute for Mathematics, Physics and Astronomy, University of Central Lancashire, Preston PR1 2HE, United Kingdom*

 (Received 18 December 2022; revised 2 March 2023; accepted 21 April 2023; published 3 May 2023)

Magnon eigenmodes in easy-plane antiferromagnetic insulators are linearly polarized and are not expected to carry any net spin angular momentum. Motivated by recent nonlocal spin transport experiments in the easy-plane phase of hematite, we perform a series of micromagnetic simulations in a nonlocal geometry at finite temperatures. We show that by tuning an external magnetic field, we can control the magnon eigenmodes and the polarization of the spin transport signal in these systems. We argue that a coherent beating oscillation between two orthogonal linearly polarized magnon eigenmodes is the mechanism responsible for finite spin transport in easy-plane antiferromagnetic insulators. The sign of the detected spin signal is also naturally explained by the proposed coherent beating mechanism. Our finding opens a path for on-demand control of the spin signal in a large class of easy-plane antiferromagnetic insulators.

DOI: [10.1103/PhysRevB.107.184404](https://doi.org/10.1103/PhysRevB.107.184404)

I. INTRODUCTION

On-demand control and long-distance transport of spin angular momentum in antiferromagnetic insulators (AFMIs) is among the cornerstones of modern spintronics. Negligible stray fields, operating at THz frequencies, and the lack of Joule heating in AFMI make them suitable candidates for the miniaturization of next-generation ultrafast spintronic-logic devices [1,2].

In collinear AFMIs with uniaxial easy-axis magnetic anisotropy, such as hematite below the Morin transition temperature [3], two circularly polarized magnon eigenmodes have opposite helicity. Each circularly polarized magnon mode carries one unit of spin angular momentum $\pm\hbar$. This spin angular momentum can be transported across micrometer distances, as recently demonstrated in nonlocal spin detection experiments in the easy-axis collinear phase of hematite α -Fe₂O₃ [4,5]. The sign of the spin accumulation in nonlocal spin transport measurements encodes the polarization of the transmitted spin angular momentum via magnons.

On the contrary, the two orthogonal magnon eigenmodes in the easy-plane AFMIs are linearly polarized and thus typically do not carry any net spin angular momentum. However, recently, Refs. [6–10] reported the transport of spin angular momentum on the micrometer scale in the easy-plane phase of hematite. Above the Morin transition temperature, hematite is a canted AFMI or weak ferromagnet with easy-plane anisotropy [3]. Some of these experiments also showed a magnetic field and spatial-dependent sign change of the spin accumulation, and thus of the magnon polarization [8,10].

In Refs. [6,7], the authors attributed the detected finite spin angular momentum transport to a birefringencelike mechanism. Within this framework, the origin of the sign change of the spin signal remained unknown. On the other hand, in Refs. [10,11] the authors attributed both finite spin angular momentum transport and the change in the sign of the spin signal to a Hanle-like behavior of the magnon pseudospin. However, within their formalism, the coupling between a small magnetization, induced by a homogeneous Dzyaloshinskii-Moriya (DM) interaction, and applied transverse magnetic field plays a crucial role in explaining the sign change of the spin signal [10,12].

In this paper, we perform finite-temperature micromagnetic simulations to study the spin angular momentum transport mechanism as well as the distance- and magnetic-field-dependent sign change of the spin signal in easy-plane AFMI systems. We explain our numerical observations with a coherent beating mechanism between two linearly polarized AFM magnon eigenmodes. We argue that both the finite spin transport and the magnetic field- and spatial-dependent sign of the spin signal are generic features of all easy-plane AFMIs and not only weak ferromagnets or canted AFMIs with a finite DM interaction, such as easy-plane hematite.

This paper is organized as follows. After introducing our model and simulation technique in Sec. II, we will first demonstrate the modulation of the magnon dispersion relation through an external magnetic field in Sec. III A. Second, in Sec. III B we will propose our coherent beating oscillation mechanism that is based on the pairing of magnons on the two dispersion branches, and demonstrate signatures of these pairs numerically in Sec. III C. Using this established model, we explain the numerically obtained spin transport signal and its oscillatory nature in Sec. III D. Finally, we conclude our findings in Sec. IV.

*verena.j.brehm@ntnu.no

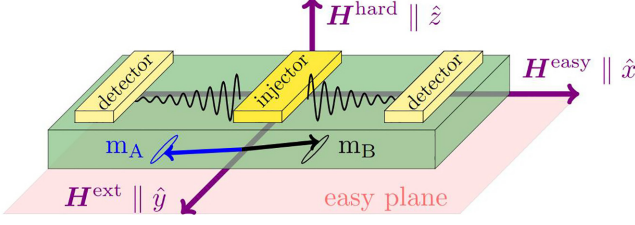


FIG. 1. Schematic presentation of the setup. Spin current is injected into an easy-plane AFMI (green region) by the central electrode via spin Hall torque and measured by the electrodes on the left and right via the inverse spin Hall effect. Purple arrows show the orientation of easy \mathbf{H}^{easy} and hard \mathbf{H}^{hard} magnetic anisotropy fields. \mathbf{H}^{ext} is a transverse external magnetic field, used to modulate the spin transport signal. The black and blue arrows show the two AFM sublattices with elliptical precession.

II. MODEL

A. System setup

We model a thin layer of AFMI in an orthorhombic phase using two anisotropy axes (see Fig. 1). The hard-axis anisotropy is set along the z direction, which gives an easy-plane magnetic anisotropy in the sample plane (x - y plane). A much weaker easy-axis magnetic anisotropy lies within the easy plane and gives a defined ground state along the x direction. In addition, a transverse magnetic field, $\mathbf{H}^{\text{ext}} = H_y \hat{y}$, perpendicular to both the easy and hard magnetic anisotropy axis, is applied to modulate the AFM magnon dispersion, as shown later. Besides, we add a homogeneous DM interaction parallel to the hard axis, and investigate its effect on the magnon dispersion and transport.

In order to simulate spin transport, magnons are pumped in the center via a spin Hall spin-transfer torque and propagate along the x direction to the left and right. The spin signal is recorded with detectors that are placed at various distances along the x direction. The polarization- and distance-dependent spin transport signal is recorded for each strength of the transverse magnetic field H_y .

Without loss of generality, we use easy-plane hematite parameters in our micromagnetic simulations. The simulation parameters [13] are listed in Table I. The characteristic length scales, at zero magnetic field, given by the exchange stiffness and the anisotropy constants $\lambda_l = \sqrt{A_{\text{AFM}}/(2K_l)}$, are $\lambda_{\text{hard}} \approx 43$ nm and $\lambda_{\text{easy}} \approx 1.35$ μm for the hard- and easy-axis anisotropies, respectively. In order to avoid the reflection of magnons at the edges of the system, we use a Gilbert damping parameter and system length that ensure the excitation decays to zero before.

B. Micromagnetic simulations

Finite-temperature simulations are conducted using a stochastic micromagnetic framework implemented in the open-source code BORIS [14]. Within the micromagnetic assumption, every discrete simulation cell with a volume V is assigned a macrospin magnetic moment \mathbf{M} with a homogeneous saturation magnetization M_s by averaging over all magnetic contributions [15]. Under the influence of temperature T , the dynamics of the magnetic moment direction $\mathbf{m} = \mathbf{M}/M_s$, in a two-sublattice AFMI, is described by

TABLE I. Micromagnetic parameters of hematite, used for simulations.

Quantity	Symbol	Value	Unit
Length of AFMI layer	L_x	2.5	μm
Width of AFMI layer	L_y	0.1	μm
Thickness of AFMI layer	L_z	5	nm
Grid size	a	5	nm
Exchange stiffness	A_{AFM}	76	fJ m^{-1}
Homogeneous exchange	a_{AFM}	-460	kJ m^{-3}
Easy-axis anisotropy	K_{easy}	-21	mJ m^{-3}
Hard-axis anisotropy	K_{hard}	21	J m^{-3}
Saturation magnetization	M_s	2.1	kA m^{-1}
Gilbert damping	α	2×10^{-4}	1
Homogeneous DM interaction	D	4.6	kJ m^{-3}
Time step	Δt	$1 @ T = 0$ $0.5 @ T \neq 0$	fs
Charge current density for SOT	J_c	560	MA m^{-2}

coupled stochastic Landau-Lifshitz-Gilbert (sLLG) equations,

$$d_i \mathbf{m}_i = -\gamma \mathbf{m}_i \times (\mathbf{H}_i^{\text{eff}} + \mathbf{H}_i^{\text{th}}) - \alpha \gamma \mathbf{m}_i \times [\mathbf{m}_i \times (\mathbf{H}_i^{\text{eff}} + \mathbf{H}_i^{\text{th}})], \quad (1)$$

where $i \in \{A, B\}$ refers to two AFM sublattices. We use $\gamma = \mu_0 |\gamma_e| / (1 + \alpha^2)$ with the vacuum permeability μ_0 , the electron gyromagnetic ratio $\gamma_e = -g\mu_B/\hbar$ with the electron g -factor g and the Bohr magneton μ_B , the reduced Planck constant \hbar , and the dimensionless Gilbert damping parameter α [16].

$\mathbf{H}_i^{\text{eff}}$ denotes the effective magnetic field at the magnetic site i , and \mathbf{H}_i^{th} is a stochastic thermal field that adds temperature to the model. For the latter, a normalized Gaussian distribution is scaled with the prefactor $\xi_{\text{th}} = \sqrt{2\alpha k_B T / (\gamma \mu_0 M_s V \Delta t)}$ in every component adding white noise to the system that is weighted with the thermal energy $k_B T$, with k_B the Boltzmann constant, and scaled with both the cell size volume V and the time step of the simulation Δt .

In our model, the effective magnetic field is given by

$$\mathbf{H}_i^{\text{eff}} = \mathbf{H}_i^{\text{ex}} + \mathbf{H}_i^{\text{DM}} + \mathbf{H}_i^{\text{aniso}} + \mathbf{H}_i^{\text{ext}} + \mathbf{H}_i^{\text{SOT}}. \quad (2)$$

\mathbf{H}_i^{ex} is the sum of homogeneous and inhomogeneous exchange interactions [14],

$$\mathbf{H}_i^{\text{ex}} = -\frac{4a_{\text{AFM}}}{\mu_0 M_s} [\mathbf{m}_i \times (\mathbf{m}_i \times \mathbf{m}_j)] + \frac{2A_{\text{AFM}}}{\mu_0 M_s} \nabla^2 \mathbf{m}_i, \quad (3)$$

where $i \neq j$, a_{AFM} is the homogeneous exchange constant, and A_{AFM} is the AFM exchange stiffness.

\mathbf{H}_i^{DM} is the homogeneous DM interaction field [14],

$$\mathbf{H}_i^{\text{DM}} = -\eta_i \frac{D}{\mu_0 M_s} \mathbf{d}_h \times \mathbf{m}_j, \quad (4)$$

where $\eta_{A(B)} = +(-)1$, D is the homogeneous DM interaction strength, and \mathbf{d}_h is the direction of the DM vector.

$\mathbf{H}_i^{\text{aniso}}$ is the anisotropy field [14],

$$\mathbf{H}_i^{\text{aniso}} = \mathbf{H}_i^{\text{hard}} + \mathbf{H}_i^{\text{easy}} = \sum_{l \in \{\text{hard}, \text{easy}\}} \frac{2K_l}{\mu_0 M_s} (\mathbf{m}_i \cdot \hat{\mathbf{e}}_l) \hat{\mathbf{e}}_l, \quad (5)$$

where the hard-axis anisotropy is given by $K_{\text{hard}} > 0$ and $\hat{e}_{\text{hard}} = \hat{z}$, and the easy-axis anisotropy is along $\hat{e}_{\text{easy}} = \hat{x}$ with $K_{\text{easy}} < 0$.

$\mathbf{H}_i^{\text{ext}}$ is the external magnetic field that couples to AFM spins via a Zeeman coupling mechanism. In our simulations, we apply a dc magnetic field perpendicular to both the easy-axis and the hard-axis anisotropy fields, i.e., along the y direction. Therefore we call it a transverse magnetic field H_y .

Finally, $\mathbf{H}_i^{\text{SOT}}$ is the total spin-orbit torque (SOT), which is the sum of a fieldlike and a dampinglike torque [14],

$$\mathbf{H}_i^{\text{SOT}} = -\frac{\Theta}{\gamma M_s} \frac{\mu_B}{e} \frac{|J_c|}{L_z} (\mathbf{m}_i \times \mathbf{P} + r_G \mathbf{P}), \quad (6)$$

generated by a charge current with the density J_c that is converted to a spin current via the spin Hall effect. \mathbf{P} is the direction of spin-Hall-induced spin polarization at the interface. Furthermore, Θ is the spin Hall angle, a measure of the efficiency of the spin-to-charge current conversion, and r_G parametrizes the fieldlike torque amplitude.

In order to model the spin-Hall-induced SOT (see Fig. 1), we set $\Theta > 0$ in the injector region, that lies in the center of the system and has an area of $6 \times 10^{-15} \text{ m}^2$, and $\Theta = 0$ otherwise. The direction of \mathbf{P} lies along the easy axis so that there is no excitation at zero temperature since $\mathbf{m}_i \parallel \mathbf{P}$. Finite temperature, however, induces thermal fluctuations in magnetic moments \mathbf{m}_i and therefore the net spin torque is finite, and consequently magnons are pumped into the AFMI layer.

C. Measurement of spin accumulation

The magnon spin current is measured at detectors by means of the inverse spin Hall effect. The inverse spin Hall voltage is proportional to the spin accumulation at the interface of the detectors and the AFMI layer, given by [17,18]

$$\mu(d) := G_r^{\uparrow\downarrow} \left\langle \sum_i [\mathbf{m}_i(t, d) \times \dot{\mathbf{m}}_i(t, d)] \right\rangle, \quad (7)$$

where $G_r^{\uparrow\downarrow}$ is the real part of the spin mixing conductance [19], $\langle \cdot \rangle$ denotes an average over both time and the ensemble, and d is the distance between the injector and detector. The time average for each ensemble member starts after steady state is reached, and afterwards, the ensemble average is taken over all spin accumulation signals. In our setup geometry, (Fig. 1), the inverse spin Hall detector measures only the x component of the spin accumulation at the interface, μ_x .

The total spin accumulation along the direction of the magnon propagation can also be expressed as $\mu_x = N S_x$, where N is the number of magnons that decay exponentially over distance due to Gilbert damping. Furthermore, $S_x = \hbar p \epsilon$, with reduced Planck constant \hbar , is the effective spin angular momentum of a magnon mode that is proportional to the helicity or handedness ($p = \pm 1$) and ellipticity ($0 \leq \epsilon \leq 1$). For linearly polarized magnon eigenmodes the ellipticity is zero, and thus $S_x = 0$, while for circularly polarized magnon eigenmodes $S_x = \pm 1$.

III. RESULTS

First, we numerically find the magnon dispersion relation of the AFMI layer and analyze the impact of a finite

homogeneous DM interaction and transverse magnetic field on the magnon dispersion. Second, we establish a magnonic beating theory that describes spin transport based on the found magnon dispersion relations. Finally, we show numerical evidence to support our proposed theory.

A. Magnon spectra

In this part, we compute the magnon spectra of easy-plane hematite numerically using a standard approach [20] at zero temperature and the absence of any spin torque, $\mathbf{H}_i^{\text{th}} = \mathbf{H}_i^{\text{SOT}} = 0$.

Magnons in the entire magnetic Brillouin zone can be excited by a magnetic field pulse with a spatial and temporal sinc function profile $\mathbf{h}(\mathbf{r}, t) = \mathbf{h}_0 \text{sinc}(\mathbf{r}) \text{sinc}(t)$, where \mathbf{h}_0 is the magnetic field vector. Depending on the relative direction of the magnetic field pulse and magnetic moments, we can excite either the in-plane linearly polarized magnon modes, when $\mathbf{h}_0 \parallel \hat{z}$, or out-of-plane linearly polarized magnon modes, when $\mathbf{h}_0 \parallel \hat{y}$, in our sample geometry (see Fig. 1). The in-plane mode is associated with the easy-axis anisotropy and has a lower magnon band gap while the out-of-plane mode is associated with the hard-axis anisotropy and has a higher magnon band gap in the easy-plane phase of hematite [see Eqs. (8) and (9)].

In Fig. 2, we plot these two magnon modes related to two magnon polarization modes. Two magnon modes are almost degenerate at large wave vectors k , near the edge of magnetic Brillouin zone, while showing different frequency values close to the center of the magnetic Brillouin zone ($k \approx 0$). The difference is pronounced at zero external magnetic field [see Figs. 2(a) and 2(f)], where the magnon band gap of the high-frequency branch (at around 0.17 THz) is two orders of magnitude larger than the gap in the low-frequency branch (around 5 GHz). However, the transverse magnetic field can tune the magnon band gap and increase the lower magnon branch, while the high-frequency branch remains practically unchanged. Once the transverse magnetic field reaches some critical value H_y^c , both branches become degenerate in the entire Brillouin zone. At higher transverse magnetic fields, $H_y > H_y^c$, the order of the two branches swaps, so that the magnons of the low-frequency branch (i.e., in-plane oscillations) have a larger frequency than the magnons of the high-frequency branch (i.e., out-of-plane oscillations). Within our set of parameters, the critical field can be read from the numerical dispersion relations as around $\mu_0 H_y^c \approx 6 \text{ T}$. To obtain more insight into the nature and exact value of the critical transverse magnetic field, we compare numerical results with the magnon spectra calculated from the standard linear spin-wave theory [21,22]. The magnon band gaps or AFM resonance (AFMR) frequencies at $k = 0$ for lower (l) and higher (h) magnon modes read

$$f_0^l = \frac{\gamma_e}{2\pi M_s} \sqrt{16|a_{\text{AFM}}|K_{\text{easy}} + (M_s \mu_0 H_y)^2 - \frac{D}{2} M_s \mu_0 H_y}, \quad (8)$$

$$f_0^h = \frac{\gamma_e}{2\pi M_s} \sqrt{16|a_{\text{AFM}}|(K_{\text{hard}} + K_{\text{easy}}) - \frac{D^2}{4} - \frac{D}{2} M_s \mu_0 H_y}. \quad (9)$$

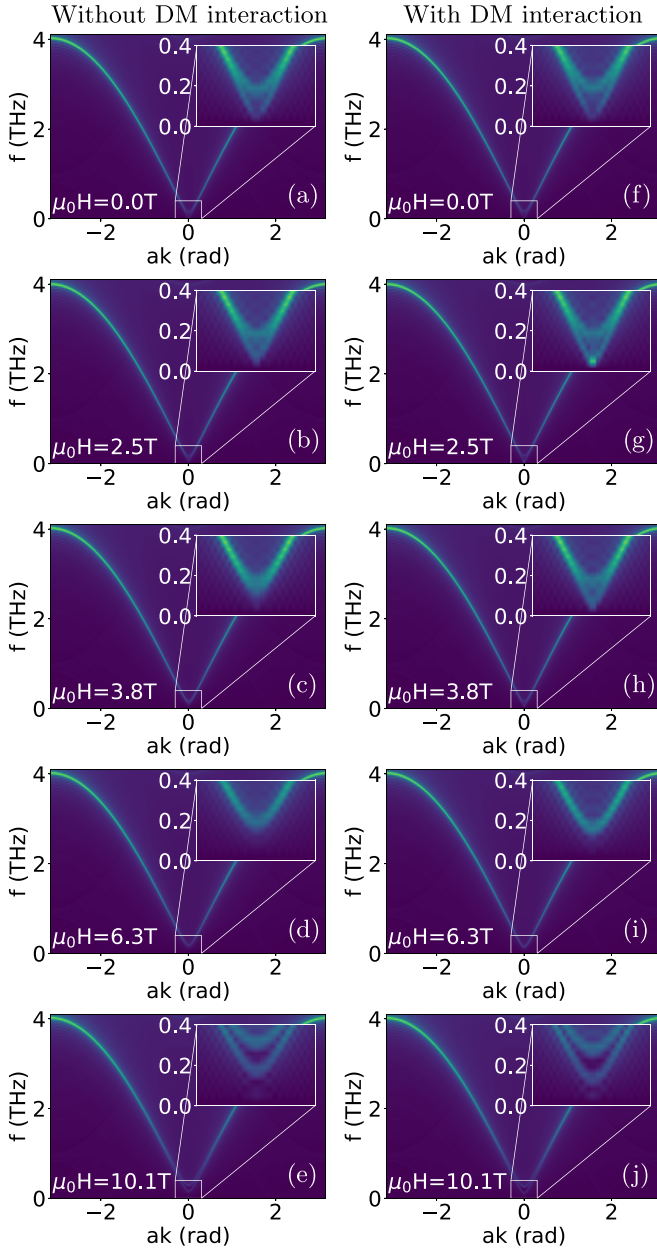


FIG. 2. Magnon dispersion relations for various transverse magnetic fields H_y without a DM interaction (left column) and with a DM interaction (right column) at $T = 0$. Without any transverse magnetic field [(a) and (f)], the two linearly polarized branches are separated by a band gap at the center of the Brillouin zone (see the inset). As the magnetic field increases, the band gap of the lower branch increases [(b), (c) and (g), (h)] until at a critical field H_y^c the band gap between the two branches is closed and they become degenerate [(d) and (i)]. Within our material parameters for hematite, the critical field is around 6 T. Above H_y^c , the order of branches is changed and a band gap reopens between the two branches [(e) and (j)].

In Fig. 3, we plot and compare the band gaps of both magnon branches with and without the homogeneous DM interaction. From Eqs. (8) and (9), we find the critical magnetic field, in which two magnon bands become degenerate, as $\mu_0 H_y^c = M_s^{-1} \sqrt{16|a_{\text{AFM}}|K_{\text{hard}} + D^2/4}$. Within the chosen material parameters, the critical magnetic field in the absence and the

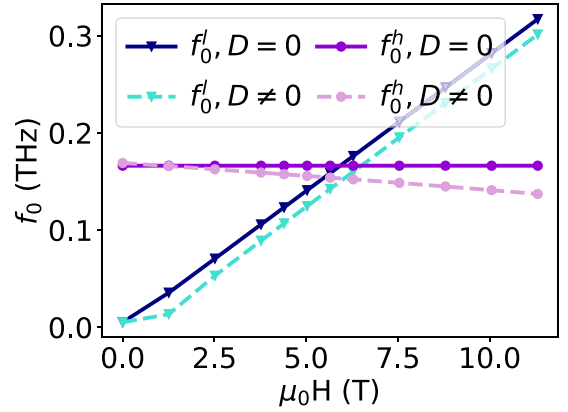


FIG. 3. AFMR amplitude as a function of the transverse magnetic field in the absence (solid lines) and presence (dashed lines) of a DM interaction. The intersection of the higher magnon branch f^h in purple dots and the lower magnon branch f^l in blue triangles shows the critical transverse magnetic field where the two magnon branches become degenerate. We conclude that the effect of a finite homogeneous DM interaction is negligible.

presence of a DM interaction is given by $\mu_0 H_y^c(D=0) \approx 5.9$ T and $\mu_0 H_y^c(D=4.6 \text{ kJ m}^{-3}) \approx 6.0$ T, respectively. The critical field can also be read in Fig. 3 as the intersection. We conclude that the effect of a homogeneous DM interaction on magnon dispersion is negligible. Therefore, we will only consider the system without a homogeneous DM interaction in the rest of this paper.

In summary, in this section, we have shown that the two magnon branches of an easy-plane AFMI can be modulated by a transverse magnetic field.

B. Coherent beating oscillation mechanism

The two magnon eigenmodes of the easy-plane hematite, shown in Fig. 2, are linearly polarized and thus cannot carry any net spin angular momentum. However, we argue that in easy-plane AFMIs still a net spin angular momentum can be carried as shown experimentally. A finite spin angular momentum can be carried by pairs of linearly polarized and orthogonal magnon eigenmodes with the same frequency but different wave numbers k_1 and k_2 , excited on two magnon branches. Due to this finite wave-number difference, a spatial-dependent oscillation of the spin transport signal emerges that, analogously to the optical counterpart phenomenon, we call magnonic coherent beating oscillation. The difference between two magnon wave numbers with the same frequency can be controlled via an applied transverse magnetic field, as shown in the previous section, and thus the beating length can be changed.

The superposition of two linearly polarized and orthogonal magnon eigenmodes with wave numbers k_1 and k_2 at the same frequency f , propagating along the x direction, is given by

$$\begin{aligned} \Psi &= \frac{1}{\sqrt{2}} \left[\chi_Z \exp(ift - ik_1 x) + \chi_Y \exp\left(ift - ik_2 x \pm i\frac{\pi}{2}\right) \right] \\ &= \frac{1}{\sqrt{2}} \chi_{ZY} \exp(ift - ik_0 x), \end{aligned} \quad (10)$$

where $\chi_Z^T = (1 \ 0 \ 0)$ and $\chi_Y^T = (0 \ 1 \ 0)$ are the transpose of the polarization eigenvectors for two linear polarization along z (out-of-plane) and y (in-plane) directions, respectively, while $\chi_{ZY}^T = (1 \ e^{i\phi_k(x)} \ 0)$ is the superposition of them in the ZY plane. We define $k_0 = k_1 + k_2$, $\Delta_k = k_1 - k_2$, and $\phi_k(x) = \Delta_k x \pm \pi/2$. The effective spin angular momentum of the wave vector is given by

$$S_x = \hbar p \epsilon = \hbar \langle \hat{J}_x \rangle \Psi = \hbar \sin \phi_k(x), \quad (11)$$

where $\hat{J}_x = \hbar \begin{pmatrix} 0 & -i & 0 \\ i & 0 & 0 \\ 0 & 0 & 0 \end{pmatrix}$ is the component of the spin-1 operator along the quantization axis in our geometry, i.e., the magnon transport direction. Therefore, the net spin angular momentum of the traveling magnon modes can continuously vary between $S_z = +(-)\hbar$, for a right- (left-)handed circularly polarized wave, and $S_z = 0$, for a linearly polarized wave, depending on $\phi_k(x)$. The distance x_0 at which the spin polarization sign is changed from left to right handed we call the magnonic beating length, $x_0 = \pi/\Delta_k$. This corresponds to the distance between a maximum and a minimum in the spin transport signal, with a zero transition at $x_0/2$, as shown in Fig. 5.

C. Band-resolved magnon population

In the previous section, we have introduced a coherent beating mechanism that is based on the excitation of pairs of magnons, where each magnon belongs to one of the branches in the dispersion relation. In order to show the evidence of these magnon pairs numerically, we compute the magnon population at low, but finite, temperature and a finite spin torque $H_i^{\text{SOT}} > 0$ in the injector region. By Fourier transforming the temporal and spatial-dependent spin configuration, we find the occupied magnon modes that contribute to the long-distance spin transport.

For our choice of parameters, i.e., the amplitude of spin torque and temperature, only low-energy magnons are excited. Thus, only the center of the Brillouin zone is shown in Fig. 4.

For small transverse magnetic fields [see Figs. 4(a) and 4(b)] and above the critical magnetic field [see Fig. 4(f)], mostly the modes in the lower magnon branch are occupied. These are linearly polarized magnon modes that cannot carry any net spin angular momentum. At these transverse magnetic field strengths, we observe a low and rapidly decaying spin transport signal (not shown).

At intermediate transverse magnetic field strengths, however, pairs of magnons with the same frequency that belong to two different magnon branches appear [see Figs. 4(c)–4(e)]. The difference in the wave numbers between two branches at one frequency, $\Delta_k = k_1 - k_2$, becomes smaller as the transverse magnetic field reaches the critical field due to the band modulation shown in Sec. III A.

D. Distance-dependent spin accumulation signal

Finally, we show the spin transport data and connect it to the proposed coherent beating oscillation theory. As we have already discussed, the detected spin signal can be written as $\mu_x(d) = \hbar N p \epsilon = \hbar N(d) \sin \phi_k(d)$. The amplitude of the

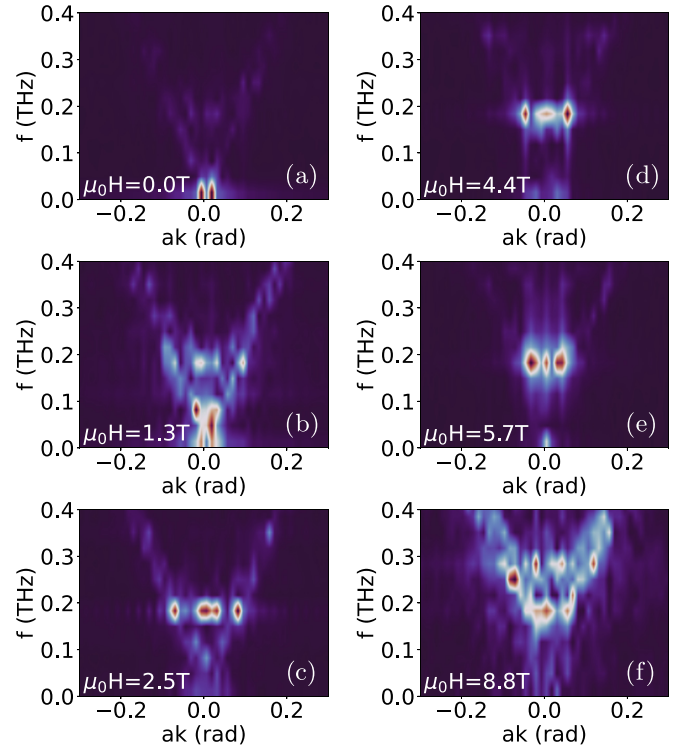


FIG. 4. Magnon modes contributing to the spin transport signal for various transverse magnetic fields at finite temperature and in the presence of the spin Hall torque. Two pairs of occupied magnon modes show up around the magnetic Brillouin zone center at intermediate strengths of the transverse magnetic field [(c)–(e)]. Each pair consists of two modes, one on each branch, at the same frequency 0.18 THz, but different wave numbers. The color map refers to the signal strength, which is proportional to the magnon occupation number, from dark meaning very low over white to red meaning very high intensity.

spin signal is proportional to the number of magnons $N(d)$ that decay exponentially with the distance d because of the Gilbert damping, and is modulated by the magnonic beating parameter $\sin \phi_k(d)$ with $\phi_k(d) = \Delta_k d \pm \pi/2$.

Figure 5 displays the numerically found distance-dependent spin accumulation in the nonlocal geometry for four different values of the transverse magnetic field H_y . Each data set is computed with an ensemble average over 20 realizations, and the uncertainty environment corresponds to the standard deviation.

As expected from the geometry, we have $\sin \phi_k(d=0) = 1$ and thus the detected spin signal is the highest close to the center, where the injector pumps spin angular momentum into the system. However, the amplitude of the spin accumulation signal does not decay exponentially, as expected from the diffusive magnon transport theory, at some transverse magnetic fields. It rather shows a damped oscillating behavior, and changes the sign periodically. At these fields, the magnon bands are nondegenerate, and thus a finite Δ_k leads to a finite beating length x_0 , which increases with increasing magnetic field (since Δ_k decreases). In order to give a quantitative example, at $\mu_0 H_y = 2.5$ T, we have $\Delta_k a = 0.06$ from Fig. 4(c), and estimate x_0 to be

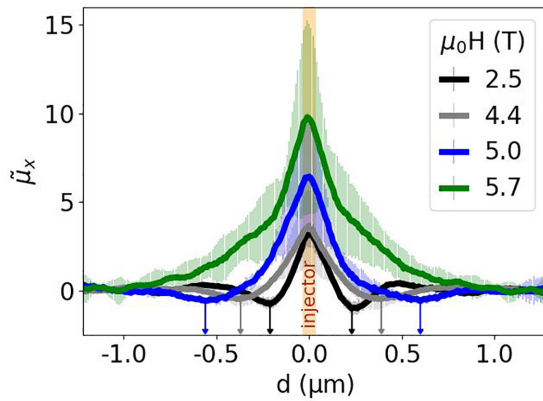


FIG. 5. Dimensionless spin accumulation signal $\tilde{\mu}_x = \mu_x(H_y, d)/\mu_x(H_y = 0, d = 0)$ along the easy-axis direction as a function of the distance between detectors and the injector, placed at the center. The transverse magnetic field H_y modulates the shape of the spin transport signal. At low magnetic fields, the sign of the spin signal polarization changes at intermediate distances. At the critical transverse magnetic field H_y^c (green curve), where the two magnon branches are degenerate, the spin signal is always positive and decays exponentially.

$x_0(2.5 \text{ T}) = 260 \text{ nm}$, which is in line with the minimum of the black curve.

On the other hand, at the critical magnetic field strength of $\mu_0 H_y \approx 5.7 \text{ T}$, where the two magnon branches are degenerate and thus the beating length diverges, $\sin(\Delta_k \rightarrow 0) = 1$,

the spin signal does not change the sign and only decays exponentially.

IV. SUMMARY AND CONCLUSION

We have found a long-distance and tunable spin transport signal in orthorhombic easy-plane AFMIs using micromagnetic simulations, in agreement with recent experimental measurements. Our model represents a large class of easy-plane AFM materials, including hematite above the Morin transition.

We demonstrated how a finite spin signal and its helicity and amplitude can be modulated by a transverse magnetic field using a coherent beating oscillation between two linearly polarized magnon eigenmodes. Based on our theoretical framework and numerical experiments, we argue that this behavior is a generic feature of all easy-plane AFMIs with two orthogonal linearly polarized eigenmodes and not only weak ferromagnets or canted AFMIs with a finite homogeneous DM interaction, such as hematite.

ACKNOWLEDGMENTS

This project has been supported by the Norwegian Financial Mechanism Project No. 2019/34/H/ST3/00515, “2Dtronics,” and partially by the Research Council of Norway through its Centres of Excellence funding scheme, Project No. 262633, “QuSpin.” The team in Mainz acknowledges support by the DFG (SFB SPIN+X No. 268565370).

- [1] V. Baltz, A. Manchon, M. Tsoi, T. Moriyama, T. Ono, and Y. Tserkovnyak, Antiferromagnetic spintronics, *Rev. Mod. Phys.* **90**, 015005 (2018).
- [2] S. Fukami, V. O. Lorenz, and O. Gomonay, Antiferromagnetic spintronics, *J. Appl. Phys.* **128**, 070401 (2020).
- [3] A. Morrish, *Canted Antiferromagnetism: Hematite* (World Scientific, Singapore, 1994).
- [4] R. Lebrun, A. Ross, S. A. Bender, A. Qaiumzadeh, L. Baldrati, J. Cramer, A. Brataas, R. A. Duine, and M. Kläui, Tunable long-distance spin transport in a crystalline antiferromagnetic iron oxide, *Nature (London)* **561**, 222 (2018).
- [5] A. Ross, R. Lebrun, O. Gomonay, D. A. Grave, A. Kay, L. Baldrati, S. Becker, A. Qaiumzadeh, C. Ulloa, G. Jakob, F. Kronast, J. Sinova, R. Duine, A. Brataas, A. Rothschild, and M. Kläui, Propagation length of antiferromagnetic magnons governed by domain configurations, *Nano Lett.* **20**, 306 (2020).
- [6] R. Lebrun, A. Ross, O. Gomonay, V. Baltz, U. Ebels, A.-L. Barra, A. Qaiumzadeh, A. Brataas, J. Sinova, and M. Kläui, Long-distance spin-transport across the Morin phase transition up to room temperature in ultra-low damping single crystals of the antiferromagnet α -Fe₂O₃, *Nat. Commun.* **11**, 6332 (2020).
- [7] J. Han, P. Zhang, Z. Bi, Y. Fan, T. S. Safi, J. Xiang, J. Finley, L. Fu, R. Cheng, and L. Liu, Birefringence-like spin transport via linearly polarized antiferromagnetic magnons, *Nat. Nanotechnol.* **15**, 563 (2020).
- [8] A. Ross, R. Lebrun, L. Baldrati, A. Kamra, O. Gomonay, S. Ding, F. Schreiber, D. Backes, F. Maccherozzi, D. A. Grave, A. Rothschild, J. Sinova, and M. Kläui, An insulat-
- ing doped antiferromagnet with low magnetic symmetry as a room temperature spin conduit, *Appl. Phys. Lett.* **117**, 242405 (2020).
- [9] A. Ross, R. Lebrun, O. Gomonay, J. Sinova, A. Kay, D. A. Grave, A. Rothschild, and M. Kläui, Magnon transport in the presence of antisymmetric exchange in a weak antiferromagnet, *J. Magn. Magn. Mater.* **543**, 168631 (2022).
- [10] T. Wimmer, A. Kamra, J. Gückelhorn, M. Opel, S. Geprägs, R. Gross, H. Huebl, and M. Althammer, Observation of Antiferromagnetic Magnon Pseudospin Dynamics and the Hanle Effect, *Phys. Rev. Lett.* **125**, 247204 (2020).
- [11] J. Gückelhorn, A. Kamra, T. Wimmer, M. Opel, S. Geprägs, R. Gross, H. Huebl, and M. Althammer, Influence of low-energy magnons on magnon Hanle experiments in easy-plane antiferromagnets, *Phys. Rev. B* **105**, 094440 (2022).
- [12] A. Kamra, T. Wimmer, H. Huebl, and M. Althammer, Antiferromagnetic magnon pseudospin: Dynamics and diffusive transport, *Phys. Rev. B* **102**, 174445 (2020).
- [13] O. R. Sulymenko, O. V. Prokopenko, V. S. Tiberkevich, A. N. Slavin, B. A. Ivanov, and R. S. Khymyn, Terahertz-Frequency Spin Hall Auto-oscillator Based on a Canted Antiferromagnet, *Phys. Rev. Appl.* **8**, 064007 (2017).
- [14] S. Lepadatu, Boris computational spintronics—High performance multi-mesh magnetic and spin transport modeling software, *J. Appl. Phys.* **128**, 243902 (2020).
- [15] C. Etz, L. Bergqvist, A. Bergman, A. Taroni, and O. Eriksson, Atomistic spin dynamics and surface magnons, *J. Phys.: Condens. Matter* **27**, 243202 (2015).

- [16] O. Eriksson, A. Bergman, L. Bergqvist, and J. Hellsvik, *Atomistic Spin Dynamics: Foundations and Applications* (Oxford University Press, Oxford, UK, 2017).
- [17] R. Cheng, J. Xiao, Q. Niu, and A. Brataas, Spin Pumping and Spin-Transfer Torques in Antiferromagnets, *Phys. Rev. Lett.* **113**, 057601 (2014).
- [18] D. Reitz, J. Li, W. Yuan, J. Shi, and Y. Tserkovnyak, Spin Seebeck effect near the antiferromagnetic spin-flop transition, *Phys. Rev. B* **102**, 020408(R) (2020).
- [19] A. Brataas, Y. V. Nazarov, and G. E. W. Bauer, Finite-Element Theory of Transport in Ferromagnet–Normal Metal Systems, *Phys. Rev. Lett.* **84**, 2481 (2000).
- [20] G. Venkat, D. Kumar, M. Franchin, O. Dmytriiev, M. Mruczkiewicz, H. Fangohr, A. Barman, M. Krawczyk, and A. Prabhakar, Proposal for a standard micromagnetic problem: Spin wave dispersion in a magnonic waveguide, *IEEE Trans. Magn.* **49**, 524 (2013).
- [21] A. Qaiumzadeh, H. Skarsvåg, C. Holmqvist, and A. Brataas, Spin Superfluidity in Biaxial Antiferromagnetic Insulators, *Phys. Rev. Lett.* **118**, 137201 (2017).
- [22] S. M. Rezende, A. Azevedo, and R. L. Rodríguez-Suárez, Introduction to antiferromagnetic magnons, *J. Appl. Phys.* **126**, 151101 (2019).